ACS NANO

www.acsnano.org

ARTICLE

Probing Charge Accumulation at $SrMnO_3$/$SrTiO_3$ Heterointerfaces via Advanced Electron Microscopy and Spectroscopy

Hongguang Wang,* Vesna Srot, Xijie Jiang, Min Yi, Yi Wang, Hans Boschker, Rotraut Merkle, Robert W. Stark, Jochen Mannhart, and Peter A. van Aken

Cite This: *ACS Nano* 2020, 14, 12697−12707

Read Online

ACCESS | Metrics & More | Article Recommendations | Supporting Information

ABSTRACT: The last three decades have seen a growing trend toward studying the interfacial phenomena in complex oxide heterostructures. Of particular concern is the charge distribution at interfaces, which is a crucial factor in controlling the interface transport behavior. However, the study of the charge distribution is very challenging due to its small length scale and the intricate structure and chemistry at interfaces. Furthermore, the underlying origin of the interfacial charge distribution has been rarely studied in-depth and is still poorly understood. Here, by a combination of aberration-corrected scanning transmission electron microscopy (STEM) and spectroscopy techniques, we identify the charge accumulation in the $SrMnO_3$ (SMO) side of $SrMnO_3$/$SrTiO_3$ heterointerfaces and find that the charge density attains the maximum of 0.13 ± 0.07 e^-/unit cell (uc) at the first SMO monolayer. Based on quantitative atomic-scale STEM analyses and first-principle calculations, we explore the origin of interfacial charge accumulation in terms of epitaxial strain-favored oxygen vacancies, cationic interdiffusion, interfacial charge transfer, and space-charge effects. This study, therefore, provides a comprehensive description of the charge distribution and related mechanisms at the SMO/STO heterointerfaces, which is beneficial for the functionality manipulation via charge engineering at interfaces.

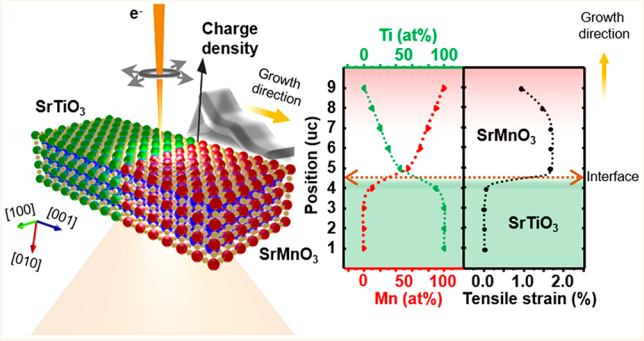

KEYWORDS: *heterointerface, oxygen vacancy, charge density, electron energy-loss spectroscopy, aberration-corrected scanning transmission electron microscopy*

Heterointerfaces in complex metal oxides promote emergent physical phenomena that are not found in their bulk constituents due to the often-cited interplay of charge, spin, orbital, and lattice degrees of freedom.[1−5] One of the cornerstone mechanisms is the charge distribution at a heterointerface.[4,6,7] Previous researchers have demonstrated that the concentration and distribution of charge can produce intriguing phenomena, e.g., enhanced ionic conductivity,[8] metallicity,[9] two-dimensional electron gases (2DEGs),[10,11] and ferromagnetism.[12] For example, the provoked charge transfer has been found to trigger a transition of the $SrMnO_3$ heterostructure from a G-type antiferromagnetic state to a ferromagnetic state.[13−15] Therefore, a comprehensive understanding of the charge distribution and their formation mechanisms at the interface is necessary for engineering the functionalities of complex oxide heterostructures.

To date, many efforts have been devoted to figuring out the interfacial charge state and its impact on the properties of materials. However, this task is still technically challenging, (i) because the characteristic scale for oxide interfaces is at the nanometer level, which makes direct observation of interface effects demanding, and (ii) because structural rearrangements and chemical environments at oxide interfaces are very complex. Therefore, it is difficult to extract the interfacial charge conditions by bulk-based characterization techniques.[16] With the advancement of methodologies and instrumentation, analytical STEM has become a highly suitable method to study the distribution of charges at the interface, because it can reveal the charge density and ordering at the atomic scale by electron

Received: February 21, 2020
Accepted: September 10, 2020
Published: September 10, 2020

https://dx.doi.org/10.1021/acsnano.0c01545
ACS Nano 2020, 14, 12697−12707

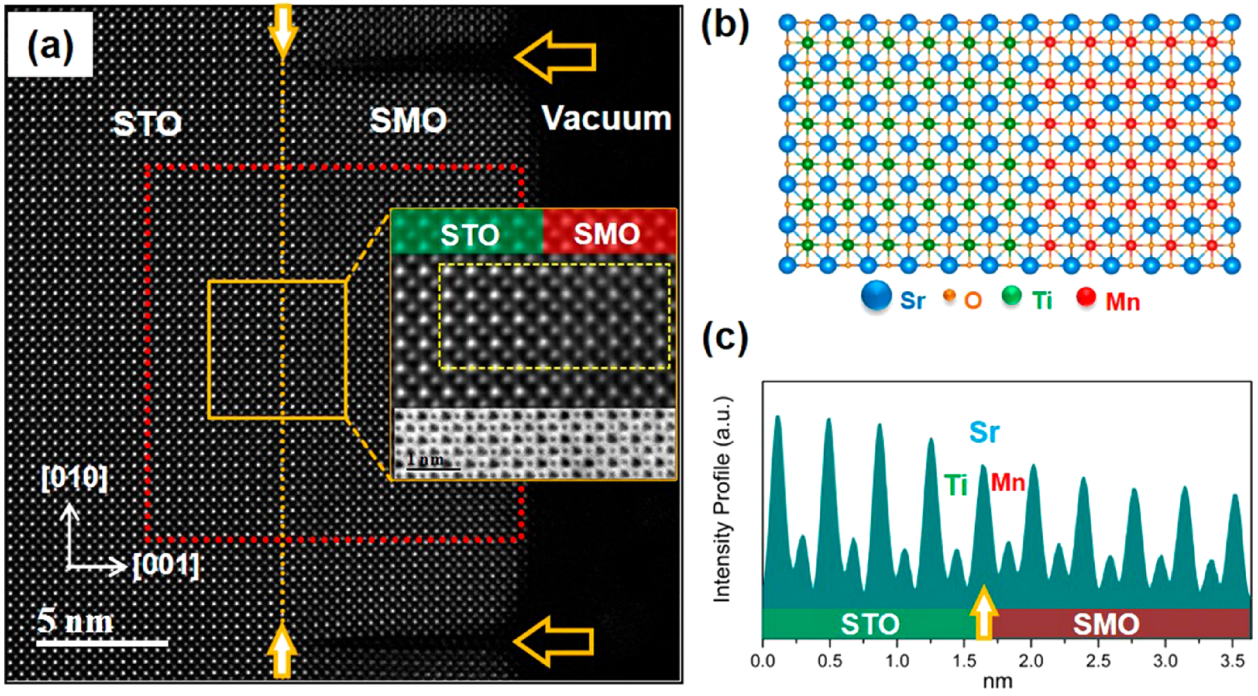

Figure 1. Microstructure of an epitaxial SMO thin film grown on an STO substrate. (a) Z-contrast HAADF-STEM image of an SMO/STO sample in cross-sectional orientation, projected along the [100] zone axis. The thickness of the SMO thin film is about 10 nm. The yellow dotted line marks the interface between SMO and STO. Horizontal arrows denote the location of cracks. The yellow box region is magnified and presented in the inset, where the upper part is a HAADF and the bottom part is an ABF image. The red square zone will be used for the strain analysis presented in Figure 3. (b) Schematic structure model of the SMO/STO interface. (c) Lateral intensity profile of the dotted box region in the inset of image (a), with the interfacial Sr column and the closest Mn and Ti columns marked according to the HAADF intensity variation.

energy-loss spectroscopy (EELS),[17−21] electron holography,[22,23] electron diffraction,[24−26] and other methods.[27,28] Among them, atomically resolved STEM-EELS has been a popular method since it enables the charge distribution and chemical environments to be measured simultaneously. Numerous studies have attempted to explore the charge distribution at the interface of manganite heterostructures with the STEM-EELS technique. However, most works were mainly focused on observations of the charge profiles and the induced properties. The formation mechanism and its association with the local structure and chemistry have been rarely explained or only referred to marginally. In a recent study, using core-loss EELS analysis, Cheng et al. identified a type of charge ordering at an interfacial MnO layer and the induced polarization of thin films, while the origin of charge ordering is only discussed from the perspective of interfacial reconstruction.[29] Likewise, Garcia-Barriocanal and co-workers examined the charge density at a manganite/titanate (LMO/STO) interface and reported a charge-leakage process controlled by the relative thickness ratio.[30] However, the detailed mechanism for the charge distribution was not explained. Therefore, it is essential to gain more insights into the detailed mechanism of interfacial charge distribution, which is vital for both fundamental understanding and application research.

In this work, epitaxial SMO thin films were grown on TiO_2-terminated (001)-oriented $SrTiO_3$ (STO) substrates by pulsed laser deposition (PLD). By using aberration-corrected STEM, we studied the structure and chemistry of the SMO films at the atomic scale and found charge accumulation at the SMO side of the interface between SMO and STO. Using STEM-based observations and first-principle calculations, we qualitatively discuss the underlying formation mechanism of charge accumulation considering the oxygen vacancies, charge transfer, and interfacial space-charge effects. Our results advance the understanding of the charge distribution at manganite interfaces, which is instructive for the fabrication of nanodevices by interfacial charge engineering.

RESULTS AND DISCUSSION

Figure 1 presents the microstructure of the epitaxial SMO/STO thin film. Two horizontal arrows in Figure 1a denote the cracks appearing in the SMO thin film. A HAADF-STEM image at lower magnification shows several nearly equidistant cracks in the SMO thin film (see Figure S1c, which are confirmed by AFM investigations (see Figure S1a,b). The cracks are caused by the relief of epitaxial strain which occurs during or after the cooling the samples after their growth.[31]

AFM measurements performed directly after growth show a flat surface of the epitaxial SMO thin film devoid of cracks (see Figure S1d). The areas between two cracks display a precise layer-by-layer stacking in the SMO thin film, as shown in the high-angle annular dark-field (HAADF) and annular bright-field (ABF) images simultaneously acquired at higher magnification, where the SMO/STO heterointerface appears coherent (Figure 1a). All atomic columns, including the oxygen ones, are resolved. The corresponding structural model of the SMO/STO interface region is displayed in Figure 1b. Based on this model, we simulated the corresponding HAADF and ABF images (see Figure S2). The simulated images show indistinguishable contrast between SMO and STO when observing with the naked eye, which is in good agreement with the experimental results. The vertically integrated HAADF

https://dx.doi.org/10.1021/acsnano.0c01545
ACS Nano 2020, 14, 12697−12707

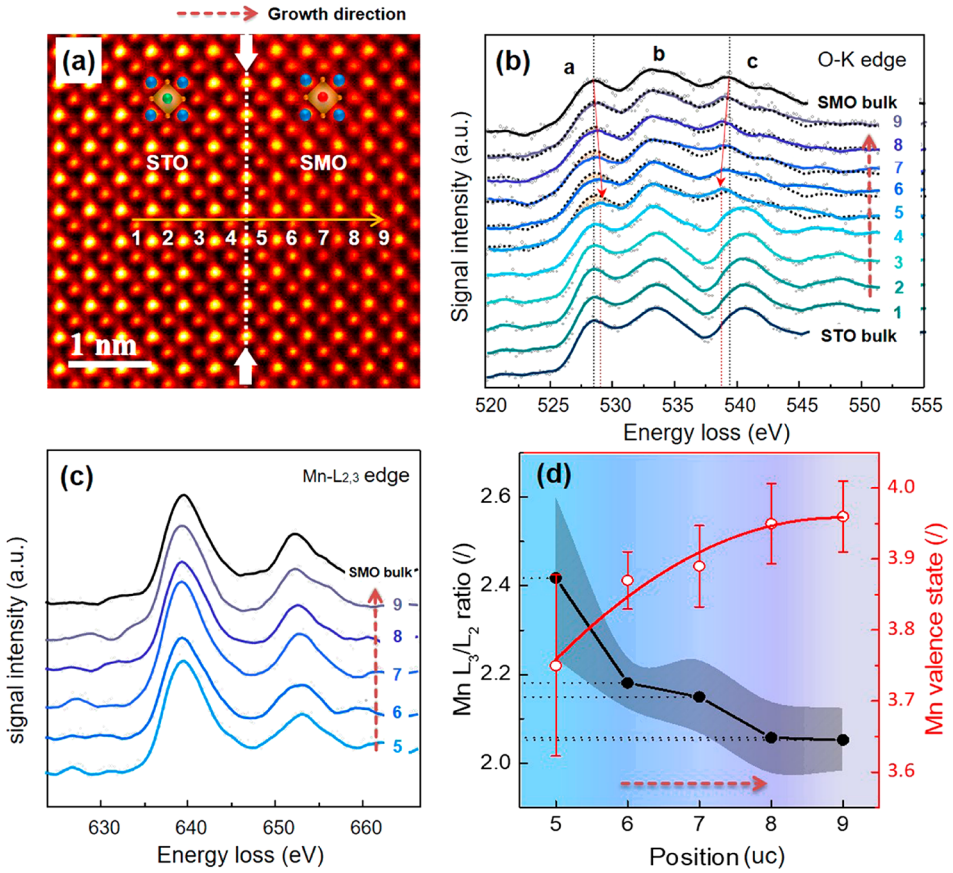

Figure 2. EELS fine structure at the heterointerface. (a) Z-contrast HAADF image of the interface region. Numbers 1 to 9 indicate the Mn (Ti)−O atomic columns across the interface, where EELS spectra were extracted. The vertical arrows mark the interface between SMO and STO. (b) O-K edge spectra for locations 1 to 9 (shown in (a)) across the interface compared with O-K edge spectra from bulk STO and SMO (black dotted lines). The dotted vertical lines mark the positions of the peak a and peak c of the O-K edge of the SMO close to the interface (red) and in the bulk state (black). (c) Mn-$L_{2,3}$ white lines for positions 5 to 9. The dotted spectra in the background represent the raw data. The backgrounds of the O-K and Mn-$L_{2,3}$ spectra have been subtracted using a power law. For removing the noise from the spectrum profiles, the raw data are fitted using a Savitzky-Golay filter with a window size of three channels and a second-order polynomial fit. (d) Mn L_3/L_2 intensity ratio (solid black circles) and the corresponding valence state (red open circles) as a function of Mn (Ti) positions (5 to 9 shown in (a)). The shaded region denotes the error bars for Mn L_3/L_2 intensity ratios, which are calculated with the standard error of the Gaussian fitting of the L_3 and L_2 edges. The errors of valence states are evaluated with the corresponding errors of intensity ratios, according to the formula of Mn valence determination.

signal within the dotted yellow box in the inset of Figure 1a is presented in Figure 1c. Since the signal intensity (I) of a HAADF image is proportional to the atomic number Z with $I = Z^{1.7}$,[32,33] the nominal interface between SMO and STO can be identified accordingly and is marked in Figure 1 by vertical arrows.

The electronic structure of the interface was explored by investigating the O-K and Mn-$L_{2,3}$ energy-loss near-edge structure (ELNES) of 9 unit cells across the heterointerface (Figure 2). Measured positions are marked in Figure 2a. Spectra 1−4 were acquired from the STO substrate and spectra 5−9 from the SMO thin film (Figure 2b). The main maxima of the O-K edge are assigned to peaks *a*, *b*, and *c*. Both Ti and Mn are surrounded by 6 O atoms in octahedral symmetry. Peak *a* of the O-K ELNES (Figure 2b) originates from the excitation of O 1s core electrons into unoccupied O p orbitals hybridized with Ti(Mn) 3d orbitals, which is sensitive to the 3d band occupancy.[31,32] Peaks *b* and *c* (Figure 2b) correspond to the hybridization of unoccupied O 2p orbitals with Sr 4d and Mn/Ti 4sp orbitals.[34,35] Here, the intensity of prepeak *a* becomes weaker than the one of the bulk SMO (dotted line) when approaching the interface from column 9 to column 5. Furthermore, we observe a gradual decrease of the energy difference between peak *a* and peak *c* while approaching the interface from spectrum 9 to spectrum 5. These observations imply a gradual reduction of the Mn valence due to an increase of the oxygen deficiency near the interface,[36−38] which presumably results from an increased number of Mn 3d electrons due to a changed structure and local chemistry around the SMO/STO interface.

Intensity ratios of L_3 and L_2 peaks of the Mn-$L_{2,3}$ ELNES (Figure 2c and Figure S3a) were calculated and are plotted in Figure 2d. From columns 5 to 9, the intensity ratios progressively decrease from ∼2.42 to ∼2.08, which are larger than the nominal value 2 for Mn^{4+}.[39] The valence states for Mn are calculated according to the Mn L_3/L_2 white-line intensity ratios[38−40] and plotted as the red profile in Figure 2d. It shows that the mean Mn valence state gradually decreases when approaching the SMO/STO interface. The valence state of Ti in STO near the interface remains nearly unchanged (see Figure S3b,c). Therefore, these results demonstrate that the

https://dx.doi.org/10.1021/acsnano.0c01545
ACS Nano 2020, 14, 12697−12707

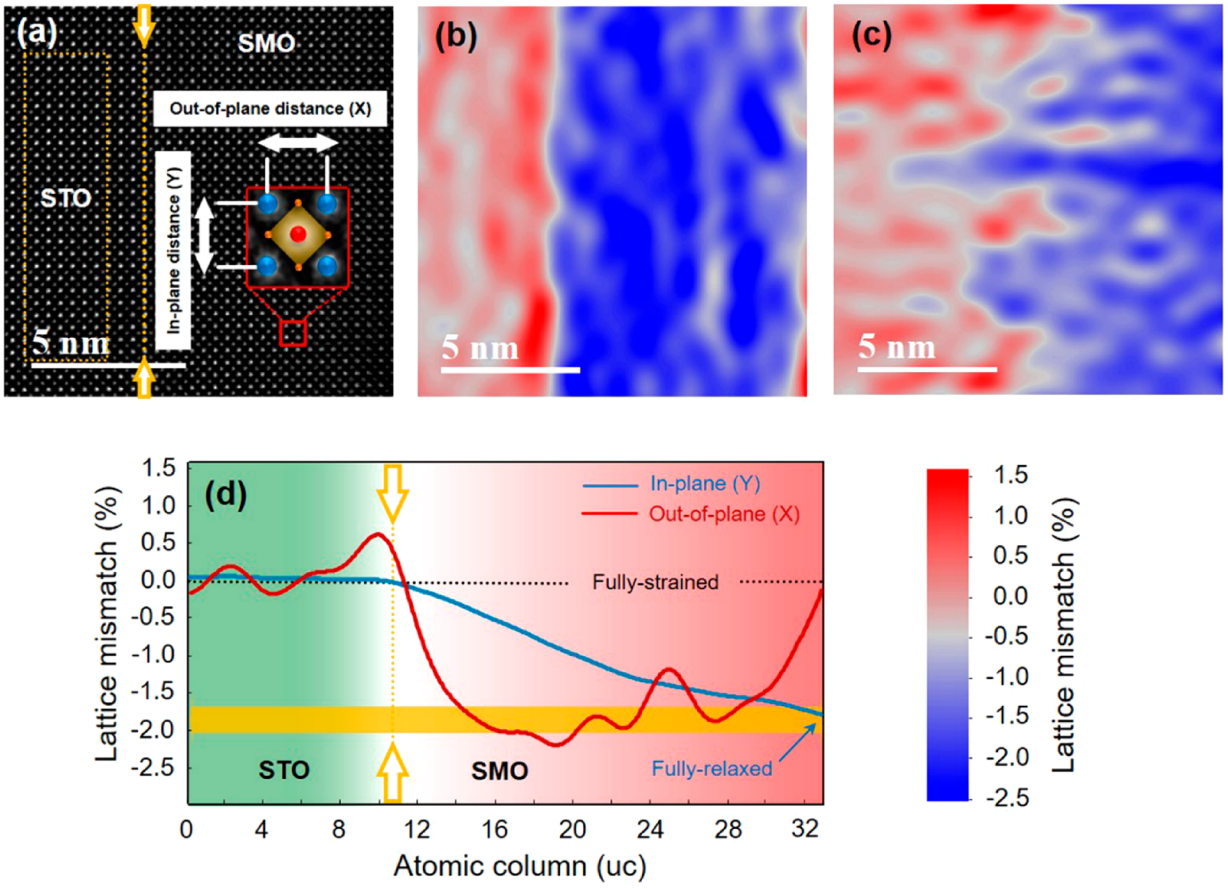

Figure 3. Strain states of the $SrMnO_3$ thin film. (a) HAADF image of a region between two cracks. The heterointerface is marked with a yellow dotted line. The box region is taken as the reference for the corresponding strain analysis. The in-plane and out-of-plane directions are defined in the inset. (b) Out-of-plane and (c) in-plane lattice mismatch for (a) with a spatial resolution of about 1.2 nm. The color bars for (b) and (c) are shown on the right side of (d). (d) Lateral intensity profile of the maps (b) and (c) with a precision of 10^{-3}.

electronic charges accumulate on the SMO side of the interface with the maximum electronic charge density in column 5.

The misfit strain can dramatically change the charge distribution at the interface and, thus, facilitate the emergence of exotic phenomena.[41] To study the strain field around the SMO/STO interface, we apply the geometric phase analysis (GPA)[42] to the atomically resolved HAADF image presented in Figure 3a. Figure 3b,c shows the 2D strain map along the out-of-plane and in-plane directions, respectively. All strain maps are produced using the $g_1 = (011)$ and $g_2 = (0\bar{1}1)$ Fourier components (see Figure S4). In the out-of-plane direction (Figure 3b), the apparent color contrast between the STO substrate and SMO thin film indicates a quick lattice relaxation owing to the free deformation along the growth direction. In contrast, the in-plane strain map in Figure 3c shows a gradual strain variation. By plotting the vertical-averaged intensity profiles of the 2D strain maps in Figure 3d, we see that the in-plane strain of the SMO thin film is progressively relaxed with increasing distance from the interface (about 1.7%) toward the SMO surface. However, due to the lateral resolution limit of the GPA-based strain analysis (about 1.2 nm in this work),[43] the exact strain state of unit cells close to the interface is not discriminable anymore.

To obtain information on the strain at the interface with atomic resolution, we fitted the atomic columns on high-resolution STEM images by a 2D Gaussian algorithm and measured the distances between atomic columns.[44] Figure 4a shows an experimental ABF-STEM image of the interface region. The corresponding coordinates of the B atom (Mn/Ti) columns were determined by 2D Gaussian fitting and were subsequently used for calculating lattice distances along the out-of-plane (ε_{xx}) and in-plane directions (ε_{yy}). Figure 4b displays the in-plane and out-of-plane lattice distances at the interfacial region, showing that the in-plane lattice distances of SMO are similar to that of the STO substrate in the first 3 unit cells close to the interface but shrink further away from the interface. The SMO lattice is still fully tensile-strained (+1.7%) along the in-plane biaxial direction in the first 3 unit cells and then gradually relaxes (+0.6% at unit cell 9). The out-of-plane lattice remains almost unchanged in SMO. According to the Poisson effect, the interfacial SMO lattice in the out-of-plane direction should be compressed due to the intense stretching of the in-plane lattice.[45] However, the corresponding change is absent in Figure 4b, which may be attributed to the presence of ions with a large radius, due to the Mn reduction or/and the elemental mixing between Mn and Ti. Additionally, the thickness of the observed TEM specimen is about 20 nm, and thus the thin foil relaxation effects become prominent.[46−48] The induced lattice relaxation along the beam direction together with the crack-induced lateral relaxation form a 3-dimensional relaxation, which may account for the absence of out-of-plane compression of the SMO lattice around the heterointerface.

https://dx.doi.org/10.1021/acsnano.0c01545
ACS Nano 2020, 14, 12697−12707

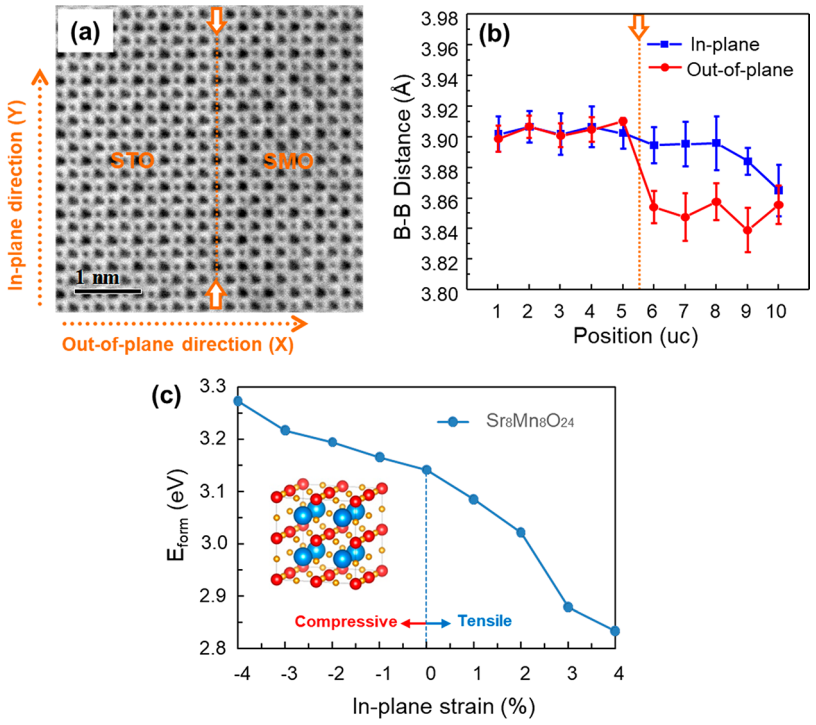

Figure 4. Interfacial strain fields and calculated formation energy of oxygen vacancies. (a) Experimental ABF-STEM image of the interface region. Vertical arrows mark the interface between SMO and STO. (b) Corresponding B (Mn/Ti)−B (Mn/Ti) atomic column spacings along the in-plane and out-of-plane directions. The error bars represent standard error with respect to averaging for each lattice layer parallel to the interface in (a). (c) Calculated formation energy E_{form} of oxygen vacancies in the SMO lattice under different in-plane biaxial strains.

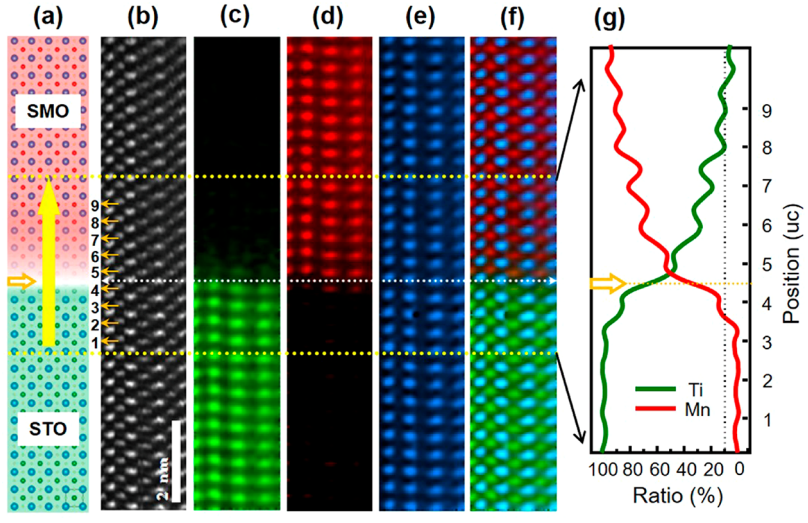

Figure 5. Atomically resolved elemental distribution at the heterointerface determined from STEM-EELS investigations. (a) Schematic of the structure at the heterointerface. The horizontal arrow marks the interface; the vertical arrow shows the region for elemental signal quantification. (b) Experimental ADF image, wherein 9 unit cells are marked. (c), (d), and (e) correspond to Ti-$L_{2,3}$ (green), Mn-$L_{2,3}$ (red), and Sr-L_3 (blue) elemental maps, where black represents zero counts of the signal. (f) Superimposed color-coded image of (c), (d), and (e). (g) Normalized Mn (red) and Ti (green) profile at the B atom position in the vicinity of the heterointerface. Position 5 is the first Mn column in the SMO thin film at the interface. Note that these maps do not provide the absolute chemical contributions but merely the relative concentration.

First-principles calculations on the formation energy of oxygen vacancies in the SMO lattice under different strain strength were performed by using a 2 × 2 × 2 SMO supercell (i.e., $Sr_8Mn_8O_{24}$). Given the fact that we investigate an interface between oxides with the same perovskite structure, it is reasonable to use bulk calculations with adjusted lattice parameters as a first approximation for the situation at a strained interface; see, e.g., refs 49−53. The formation energy of one oxygen vacancy in these strained supercells was evaluated. Figure 4c shows the results calculated for various in-plane biaxial strains, with a = 3.84 Å (the relaxed in-plane lattice parameter at the SMO surface) as the zero-strain state. The oxygen-vacancy formation energy changes approximately linearly as a function of the strain. It decreases from about 3.3

https://dx.doi.org/10.1021/acsnano.0c01545
ACS Nano 2020, 14, 12697−12707

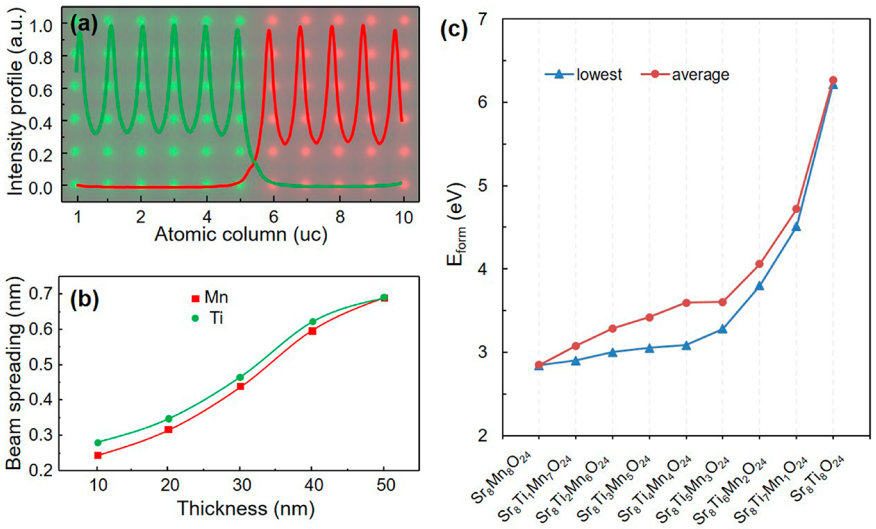

Figure 6. Beam spreading effects on the SMO/STO heterointerface and cation-intermixing-induced formation of oxygen vacancies. (a) Simulated 2D EEL spectrum image for the Ti-$L_{2,3}$ edge (green) and the Mn-$L_{2,3}$ edge (red). This spectrum image was obtained using the thickness of our sample. All other simulation parameters were set according to the experimental conditions during the experimental STEM-EELS investigations. The vertically integrated intensity profiles show a sharp signal variation at the interface. (b) Signal spreading of the Ti-$L_{2,3}$ edge (green) and the Mn-$L_{2,3}$ edge (red) as a function of sample thickness. (c) Lowest and average formation energy of an oxygen vacancy obtained by first-principles calculations.

eV for a compressive strain of 4% to ca. 2.8 eV for a tensile strain of 4%. The decreasing rate shown by the Figure 4c values on average is around −0.0625 eV per 1% strain. These results indicate an enhanced formation of oxygen vacancies in the SMO film with an increase of the in-plane biaxial tensile strain.

The chemical distribution around the interface was studied by 2D STEM-EELS elemental mapping (Figure 5). A structural model of the SMO/STO interface (Figure 5a) shows the ideal atomic stacking on both sides of the interface. An experimental ADF-STEM image (Figure 5b) with corresponding elemental maps using the Ti-$L_{2,3}$ (c), Mn-$L_{2,3}$ (d), and Sr-$L_{2,3}$ (e) edges and the composite image in Figure 5f display the elemental distribution near the interface at the atomic scale.

Figure 5g shows the normalized intensity profiles between Mn and Ti, indicating that the interface is not atomically abrupt, accompanying an asymmetric cation intermixing on both sides of the interface. The diffusion length for Mn inside the STO substrate is about 1 unit cell, while it is about 4 unit cells for Ti inside the SMO thin film. Nevertheless, the observed signal spreading shown by STEM-EELS observations does not necessarily originate from the cationic intermixing in the material. The signals may result from thermal diffuse scattering, multiple scattering, and dechanneling effects of electrons, which may cause a deviation of the experimental results from the real elemental distribution in the material.[54] We will discuss these effects now in more detail.

The ratio of the sample thickness (T) and the inelastic mean free path (λ) has the main impact on signal delocalization,[55] which explains that delocalization effects in thin samples will be minimized due to weak multiple inelastic electron scattering. From the simultaneously acquired low-loss map, the sample thickness has been determined via the Fourier ratio method[56] to ca. 20 nm throughout the interface region with $T/\lambda = 0.20$ (see Figure S5).

To interpret the experimental results and determine the elemental distributions around the interface more accurately, we simulated EELS spectrum images at the SMO/STO heterointerface for various sample thicknesses with the μSTEM code, using the model for quantum excitations of phonons.[57,58] A superstructure with 11 × 6 × 64 unit cells corresponding to the same sample thickness as we studied experimentally was employed for the calculation. The interface was considered to be atomically abrupt. The spectra image obtained from the simulation is presented in Figure 6a. The plot shows the intensity profiles of the Ti-$L_{2,3}$ and Mn-$L_{2,3}$ signals across the interface, demonstrating a weak beam spreading of about 1 unit cell on both sides of the interface. Figure 6b displays the spreading of the signal as a function of the sample thickness, indicating an approximately linear relationship. There exists no prominent difference for the signal spreading between Mn and Ti due to their small difference in the atomic numbers.

Based on the experimental observations (Figure 5g) and the simulation (Figure 6b), we substantiate an asymmetric cationic distribution around the interface and verify strong elemental intermixing in the interface region. A previous study suggested that the cation intermixing induces an off-stoichiometry at the interface between the manganite and titanate.[59] Here we used first-principles calculations to evaluate the influence of cation intermixing on the formation of oxygen vacancies. As a simplified model, we take a 2 × 2 × 2 SMO supercell (i.e., $Sr_8Mn_8O_{24}$) and replace Mn atoms consecutively by the Ti atoms (see Figure S6). The lattice parameters are taken as a = 3.905 Å and c = 3.84 Å, which are the experimentally measured values for the SMO lattice close to the interface. The calculated formation energies for one oxygen vacancy at different oxygen sites are obtained (see Figure S7), revealing that the magnitude of the energy is closely linked to the Ti content, usually differing between inequivalent positions. From the lowest formation energy of oxygen vacancy in Figure 6c, we find that a concentration of 12.5% Ti in SMO slightly increases the oxygen vacancy formation energy by 0.05 eV. Only when Ti substitutes more than 50% of Mn, the formation energy of

https://dx.doi.org/10.1021/acsnano.0c01545
ACS Nano 2020, 14, 12697−12707

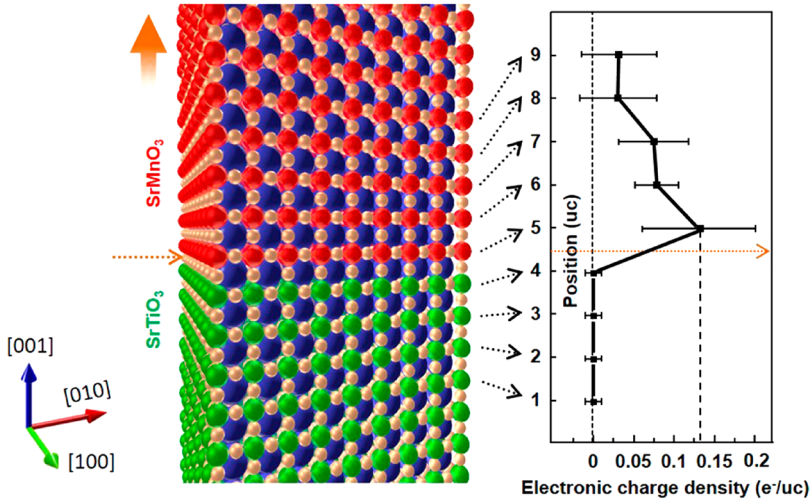

Figure 7. Electronic charge density as a function of atomic position near the interface. The horizontal dotted arrows mark the interface between SMO and STO. The error bars are determined according to the calculated error bars of the valence states.

oxygen vacancies increases sufficiently to exceed that of the pure SMO by much.

Charge Distribution and Interpretation. Based on energy-loss near-edge fine structure analysis of the Mn-$L_{2,3}$ and O-K edges (Figure 2b,c), we verified the previously observed charge accumulation at the SMO side of the interface, where the charge density attains the maximum (0.13 ± 0.07 e^-/uc) in the first SMO monolayer and becomes smaller farther from the interface (Figure 7). The charge distribution at the heterointerface is caused by a complex mechanism, which may be attributed to multiple effects such as epitaxial strain, charge transfer, interfacial space-charge layer, and cation diffusion. These differences are also strongly intertwined.

Tensile-Strain-Favored Oxygen Vacancies. Owing to the lattice mismatch between SMO (3.84 Å) and STO (3.905 Å), the epitaxial SMO film is tensile-strained. In this work, due to the appearance of cracks, tensile strain fields are partially relaxed, yielding a strain maximum in the SMO lattice close to the interface. To stabilize the SMO lattice, the electron configurations and chemical composition could be altered in the presence of strain.[49,60] In this work, on the one hand, since the ionic radius of Mn^{3+} (low spin: 0.58 Å, high spin: 0.65 Å) is larger than that of Mn^{4+} (high spin: 0.53 Å),[61] the Mn ions tend to be reduced from +4 to +3 to compensate the tensile strain imposed by the STO substrate. This valence decrease may result from the appearance of oxygen vacancies, which were reported to be enhanced by applying tensile strain fields and reduced by applying compressive strain.[53] On the other hand, the magnitude of the epitaxial strain was reported to be tunable by changing the concentration of oxygen vacancies in the SMO thin film.[62] Our first-principles calculations show that the in-plane tensile strain lowers the formation energy of oxygen vacancies in SMO (Figure 4c). This finding is consistent with previous experimental and theoretical studies,[50,53,63,64] that rationally attribute the charge accumulation at the interface to the formation of oxygen vacancies.

Interfacial Cationic Interdiffusion. Combining STEM-EELS observations and μSTEM calculations, we unambiguously verified that Mn and Ti intermix in the last 1 STO monolayer and the first 3 SMO monolayers close to the interface. In this work, the intermixing between Mn and Ti at the interface partially offsets the above-mentioned tensile strain effects on the charge accumulation, because the radius of Ti^{4+} (0.60 Å) exceeds that of Mn^{4+}(0.53 Å).[61] Meanwhile, the calculation results show that the interdiffusion between Mn and Ti changes the formation energy of the oxygen vacancies (Figure 6c). Interestingly, the cationic intermixing at the interface plays an obstructing role in the charge accumulation on the SMO side of the interface, because the substitution of Mn by Ti in the SMO enhances the formation energy of oxygen vacancies, especially for a large number of Ti substitutions. Nevertheless, as indicated by the calculation results as well, the interdiffusion between Mn and Ti could significantly favor the appearance of oxygen vacancies on the STO side of the interface (Figure 6c), making STO more conductive than naively expected.

Electron Transfer from the STO Substrate. Charge transfer occurs at the interface when the Fermi levels of the separate materials differ. For the case of the STO−SMO interface, this is relevant, because STO tends to be *n*-type conducting under the reducing conditions of PLD. This implies that the Fermi level of STO is close to the conduction band. The conduction band of STO is higher than that of SMO[15,65,66] (see also Figure S8), and therefore electrons in the conduction band of STO can move to the SMO side of the interface. In this work, we measured an electronic charge density of about 0.13 e^-/uc in the first SMO monolayer, which corresponds to 0.85×10^{14} e^-/cm^{-2}. According to the crystal growth conditions, the STO substrate is usually treated as an insulator, which implies that the charge density is supposed to be smaller than 1×10^{18} cm^{-3}.[67] If one assumes that the charge accumulation originates from the charge transfer from the STO substrate, the accumulation layer needs to collect all charges of the top 0.85 μm of the substrate, indicating that the effect of charge transfer, in this case, can be ignored. However, previous works put forward that the PLD process is efficient for removing oxygen from the material, especially at a low oxygen pressure, making the STO substrate more conductive than expected.[68,69] Therefore, the effect of an electron transfer on the observed charge accumulation cannot be ruled out. This illustrates the need to consider the effect of the PLD deposition parameters when studying the charge distribution at the interface.

https://dx.doi.org/10.1021/acsnano.0c01545
ACS Nano 2020, 14, 12697−12707

Space-Charge Effects at the Interface. Whenever the symmetry of an infinite solid ionic system is broken by introducing interfaces, space charges are a necessary consequence of the chemical difference of anions and cations reflected by different local partial free energies.[70,71] In ionic materials, the respective transfer of charged ionic defects such as oxygen vacancies can lead to perceptible excess charge densities despite a large band gap (see, e.g., data for grain boundaries in $SrTiO_3$ in ref 72). Compared to this, electronic interfacial states are of minor importance and are not further considered here. Even though we do not observe the sign of oxygen vacancies in the STO substrate from the ELNES of the O-K edge, oxygen vacancies with a density below the detection limit of EELS may exist. If we treat the interface zone as a space charge region, effective negative charges should appear in SMO to compensate for the positive charges resulting from the oxygen vacancies in STO. However, if the transition from Mn^{4+} to Mn^{3+} is fully compensated by the formation of oxygen vacancies in SMO, both sides of the interface are neutral and no space-charge effect appears.

CONCLUSIONS

By using spherical-aberration-corrected analytical scanning transmission electron microscopy, this study confirms the electronic charge accumulation on the SMO side of STO/SMO interfaces. The charge density reaches a maximum (0.13 ± 0.07 e^-/uc) at the first SMO monolayer. Through detailed experimental and theoretical investigations, this work provides a comprehensive description of the underlying mechanisms of the charge accumulation, including strain-related effects, cationic intermixing, interfacial charge transfer, and space charge effects. Taken together, our results suggest that the observed charge accumulation at the interface has multiple origins, which need to be interpreted from a comprehensive perspective. While this study focuses on one specific interface, the interface between SMO and STO, its results are of broader relevance. The data evince that the charge distribution at interfaces may well be controlled by a multitude of mechanisms, such as strain fields, local chemistry, charge transfer, and defect formation, which act on different length scales.

METHODS

$SrMnO_3$ Thin Film Preparation. The epitaxial $SrMnO_3$ thin films were grown on TiO_2-terminated (001)-oriented $SrTiO_3$ substrates (Shinkosha) by PLD using a stoichiometric, polycrystalline target (Lesker). For making the single terminated TiO_2 surface of STO substrates, the STO substrates were prepared by ultrasonification in water and then treated by a combination of etching with a buffered HF solution and *ex situ* annealing at 1050 °C.[73] The growth temperature was 800 °C, the oxygen pressure was 0.05 mbar, the laser fluency was 2 J cm^{-2}, the laser frequency was 1 Hz, and the growth rate was 0.04 monolayer per pulse. The wavelength of the KrF laser was 248 nm. The growth mode is a layer-by-layer growth as evidenced by the observation of reflection high-energy electron diffraction (RHEED) oscillations. The surface morphology was investigated by a Cypher atomic force microscope (Asylum Research, Santa Barbara, CA, U.S.A.).

Sample Preparation and STEM Investigations. TEM specimens were prepared by mechanical wedge polishing followed by Ar ion-beam milling at liquid-N_2 temperature.

SMO thin films were studied using a spherical aberration-corrected STEM (JEM-ARM200F, JEOL Co. Ltd.) equipped with a cold field emission gun and a DCOR probe C_s-corrector (CEOS GmbH) operated at 200 kV. The STEM images were obtained by JEOL ADF and BF detectors with a probe size of 0.8 Å (corresponding to the spot size 8C in the experimental setting), a convergent semiangle of 20.4 mrad, and a camera length of 6 cm. The corresponding collection semiangles for HAADF imaging were 70−300 mrad and for ABF imaging 11−22 mrad. To improve the signal-to-noise ratio (SNR) and to minimize the image distortion of HAADF and ABF images, 10 serial frames were acquired with a short dwell time (2 μs/pixel), aligned and added afterward.[27] EELS acquisition was performed by a Gatan GIF Quantum ERS imaging filter with dual-EELS acquisition capability with a convergent semiangle of 20.4 mrad and a probe size of 1 Å (5C), which is larger than that of STEM imaging. While the spatial resolution becomes worse as the probe size increases, the probe current rises, allowing for enhanced EELS analysis with a higher signal-to-noise ratio. With the 1.5 cm camera length and 5 mm entrance aperture of the image filter, a collection semiangle of 111 mrad was used for EELS acquisition. Dual EELS spectrum imaging was performed with a dispersion of 1 eV/channel and 510 eV drift tube energy with a 2048 pixel wide detector for the simultaneous acquisition of the Sr, Ti, and Mn spectrum image. The SI survey image was simultaneously acquired using the Gatan ADF detector at an inner collection semiangle of 111 mrad. The raw spectrum image data were first denoised by applying PCA with a multivariate statistical analysis (MSA) plugin (HREM Research Inc.) in Gatan DigitalMicrograph and then smoothed using a spatial filter in Gatan DigitalMicrograph. The PCA process may introduce some artifacts to the maps, making the atomic columns sharper than expected.[74] The elemental maps were extracted using a standard multiple linear least-squares fitting method. The integration windows for the Sr, Mn, and Ti maps are (1871−2093) eV, (629−654) eV, and (443−478) eV, respectively. Energy-loss near-edge structure analysis was carried out with a dispersion of 0.1 eV/channel, where the energy resolution is 0.7 eV measured as the full-width at half-maximum of the zero-loss peak. Strain analysis was carried out using Geometry Phase Analysis (GPA) developed by Martin Hÿtch through a commercial GPA plugin (HREM Research Inc.) in Gatan DigitalMicrograph.

STEM-Image and STEM-EELS Spectrum-Image Simulations. STEM images of the heterointerface were simulated using a multislice method implemented in QSTEM image simulation software[75] applying the experimental parameters during STEM imaging. The QSTEM Model Builder was employed to build the interfacial structure model to match atomic columns in the experimental STEM image. Since the interface structure model was not fully relaxed by *ab initio* methods due to a too large number of atoms, the simulated images merely provide a good sanity check rather than a quantitative explanation. To examine the complex electron-scattering effects at the heterointerface, we have performed multislice STEM-EELS simulations using the μSTEM code.[58] The parameters for the spectrum-image simulations were set according to the experimental STEM-EELS conditions.

First-Principles Calculations. The formation energy of an oxygen vacancy in the SMO system was calculated using VASP (Vienna *Ab initio* Simulation Package). The generalized gradient approximation (GGA) was employed with the exchange-correlation functional of Perdew−Burke−Ernzerhof (PBE). The cutoff energy was set to 500 eV. The projector augmented wave (PAW) method was used to describe electron−core interactions with $Sr(4s^2,4p^6,5s^2)$, $Mn(3s^2,3p^6,3d^5,4s^2)$, $Ti(3s^2,3p^6,3d^2,4s^2)$, and $O(2s^2,2p^4)$ shells treated as valence electrons. For the relaxation calculation, convergence criteria for the maximum force on each atom and the total energy were 0.01 eV/Å and 5×10^{-5} eV, respectively. During the relaxation calculations in the case of in-plane strained SMO, the in-plane lattice parameters (a and b) are fixed, while the lattice parameter c and internal coordinates of all atoms are fully relaxed. In the relaxation calculations of $Sr_8Ti_xMn_{8-x}O_{24}$ (x = 0, 1, ..., 8) (as shown in Figure S6), the experimentally measured lattice parameters a = 7.81 Å and c = 7.68 Å are fixed, and the internal coordinates of all atoms are fully relaxed. In the self-consistent calculations of the total energy, an energy convergence criterion of 10^{-5} eV was used. A Coulomb interaction of U = 2.7 eV and on-site exchange interaction of J = 1.0 eV were used to treat the Mn d electrons.[51] For Ti d

https://dx.doi.org/10.1021/acsnano.0c01545
ACS Nano 2020, 14, 12697−12707

electrons, we used U = 3.2 eV, J = 0.9 eV.[76] All calculations were performed using 2 × 2 × 2 supercells constructed from an orthorhombic unit cell with five atoms.[51] The convergence test indicated that the 5 × 5 × 5 Γ-centered k mesh was sufficient. The oxygen vacancy formation energy E_{form} was computed by $E_{form} = E^{vo} + E^{\circ} - E^{noVo}$, in which E^{Vo}, E°, and E^{noVo} denote the total energy of supercell with one oxygen vacancy, an oxygen atom, and supercell without oxygen vacancy, respectively. Since we used a simplified structural model to mimic the interfacial structure, the calculated formation energy of the oxygen vacancy may be higher than in a real interface structure. Nevertheless, the trends for the formation energy in the case of strain and elemental intermixing are, in principle, the same.

ASSOCIATED CONTENT

Supporting Information

The Supporting Information is available free of charge at https://pubs.acs.org/doi/10.1021/acsnano.0c01545.

More details about the surface morphology of the SMO thin film, low-magnification STEM imaging of the specimen cross-section, HAADF and ABF image simulation at the heterointerface, spectra of the Ti-$L_{2,3}$ edge close to the interface, strain analysis at the interface, thickness mapping by low loss spectra, first-principle calculations of the formation energy of oxygen vacancies, and the calculated density of states of the Sr(Mn, Ti)O_3 supercells (PDF)

AUTHOR INFORMATION

Corresponding Author

Hongguang Wang − *Max Planck Institute for Solid State Research, 70569 Stuttgart, Germany;* orcid.org/0000-0001-8552-2323; Email: hgwang@fkf.mpg.de

Authors

Vesna Srot − *Max Planck Institute for Solid State Research, 70569 Stuttgart, Germany;* orcid.org/0000-0001-8864-0931

Xijie Jiang − *Institute of Materials Science, Technische Universität Darmstadt, 64287 Darmstadt, Germany*

Min Yi − *Institute of Materials Science, Technische Universität Darmstadt, 64287 Darmstadt, Germany; State Key Lab of Mechanics and Control of Mechanical Structures, Nanjing University of Aeronautics and Astronautics (NUAA), Nanjing 210016, China*

Yi Wang − *Max Planck Institute for Solid State Research, 70569 Stuttgart, Germany*

Hans Boschker − *Max Planck Institute for Solid State Research, 70569 Stuttgart, Germany*

Rotraut Merkle − *Max Planck Institute for Solid State Research, 70569 Stuttgart, Germany;* orcid.org/0000-0003-3811-8963

Robert W. Stark − *Institute of Materials Science, Technische Universität Darmstadt, 64287 Darmstadt, Germany*

Jochen Mannhart − *Max Planck Institute for Solid State Research, 70569 Stuttgart, Germany*

Peter A. van Aken − *Max Planck Institute for Solid State Research, 70569 Stuttgart, Germany*

Complete contact information is available at: https://pubs.acs.org/10.1021/acsnano.0c01545

Author Contributions

H.G.W. carried out the TEM specimen preparation, TEM data acquisition, and TEM-related simulation with the help from V. S. and Y.W. H.G.W. performed data processing and wrote the manuscript. M.Y. did the first-principle calculations, analyzed the results, and contributed to writing the manuscript. X.J. performed the AFM measurement and further data analysis. H.B. grew the SMO thin films. R.M. contributed to the discussion part of the manuscript. P.A.v.A., J.M., and R.W.S. supervised and oversaw this work. All the authors discussed the results and contributed to the final manuscript.

Notes

The authors declare no competing financial interest.

ACKNOWLEDGMENTS

H.G.W. thanks the China Scholarship Council for a Ph.D. scholarship (No. 201504910813), the Max Planck Society for financial support, and the support from the Stuttgart Center for Electron Microscopy (StEM) at the Max Planck Institute for Solid State Research. M.Y. acknowledges the support from the 15th Thousand Youth Talents Program of China, German Science Foundation (DFG YI 165/1-1), NSFC (11902150), the Research Fund of State Key Laboratory of Mechanics and Control of Mechanical Structures (MCMS-I-0419G01), and the access to the Lichtenberg High-Performance Computer of the TU Darmstadt. The authors gratefully acknowledge the insightful discussion with W. Sigle, support during TEM sample preparation by U. Salzberger and M. Kelsch, and the TEM support by K. Hahn and P. Kopold. This project has received funding from the European Union's Horizon 2020 research and innovation programme under Grant Agreement No. 823717 − ESTEEM3.

REFERENCES

(1) Mannhart, J.; Schlom, D. Oxide Interfaces-An Opportunity for Electronics. *Science* **2010**, *327*, 1607−1611.

(2) Dagotto, E. PHYSICS. When Oxides Meet Face to Face. *Science* **2007**, *318*, 1076−1077.

(3) Ramesh, R.; Schlom, D. G. Creating Emergent Phenomena in Oxide Superlattices. *Nat. Rev. Mater.* **2019**, *4*, 257−268.

(4) Hwang, H. Y.; Iwasa, Y.; Kawasaki, M.; Keimer, B.; Nagaosa, N.; Tokura, Y. Emergent Phenomena at Oxide Interfaces. *Nat. Mater.* **2012**, *11*, 103−113.

(5) Chakhalian, J.; Millis, A. J.; Rondinelli, J. Whither the Oxide Interface. *Nat. Mater.* **2012**, *11*, 92−4.

(6) Gunkel, F.; Waser, R.; Ramadan, A. H. H.; De Souza, R. A.; Hoffmann-Eifert, S.; Dittmann, R. Space Charges and Defect Concentration Profiles at Complex Oxide Interfaces. *Phys. Rev. B: Condens. Matter Mater. Phys.* **2016**, *93*, 245431.

(7) Caprara, S. Oxide Interfaces: Spin-to-Charge Current Conversion. *Nat. Mater.* **2016**, *15*, 1224−1225.

(8) Sata, N.; Eberman, K.; Eberl, K.; Maier, J. Mesoscopic Fast Ion Conduction in Nanometre-Scale Planar Heterostructures. *Nature* **2000**, *408*, 946−949.

(9) Ohtomo, A.; Muller, D. A.; Grazul, J. L.; Hwang, H. Y. Artificial Charge-Modulationin Atomic-Scale Perovskite Titanate Superlattices. *Nature* **2002**, *419*, 378−80.

(10) Ohtomo, A.; Hwang, H. Y. A High-Mobility Electron Gas at the $LaAlO_3/SrTiO_3$ Heterointerface. *Nature* **2004**, *427*, 423−426.

(11) Mannhart, J.; Blank, D. H. A.; Hwang, H. Y.; Millis, A. J.; Triscone, J. M. Two-Dimensional Electron Gases at Oxide Interfaces. *MRS Bull.* **2008**, *33*, 1027−1034.

(12) Brinkman, A.; Huijben, M.; Van Zalk, M.; Huijben, J.; Zeitler, U.; Maan, J. C.; Van der Wiel, W. G.; Rijnders, G.; Blank, D. H. A.;

Hilgenkamp, H. Magnetic Effects at the Interface between Non-Magnetic Oxides. *Nat. Mater.* **2007**, *6*, 493−496.
(13) Salamon, M. B.; Jaime, M. The Physics of Manganites: Structure and Transport. *Rev. Mod. Phys.* **2001**, *73*, 583−628.
(14) Tokura, Y. Critical Features of Colossal Magnetoresistive Manganites. *Rep. Prog. Phys.* **2006**, *69*, 797−851.
(15) Zhong, Z. C.; Hansmann, P. Band Alignment and Charge Transfer in Complex Oxide Interfaces. *Phys. Rev. X* **2017**, *7*, 011023.
(16) Gao, P.; Ishikawa, R.; Feng, B.; Kumamoto, A.; Shibata, N.; Ikuhara, Y. Atomic-Scale Structure Relaxation, Chemistry and Charge Distribution of Dislocation Cores in $SrTiO_3$. *Ultramicroscopy* **2018**, *184*, 217−224.
(17) Phillips, P. J.; Rui, X.; Georgescu, A. B.; Disa, A. S.; Longo, P.; Okunishi, E.; Walker, F.; Ahn, C. H.; Ismail-Beigi, S.; Klie, R. F. Experimental Verification of Orbital Engineering at the Atomic Scale: Charge Transfer and Symmetry Breaking in Nickelate Heterostructures. *Phys. Rev. B: Condens. Matter Mater. Phys.* **2017**, *95*, 205131.
(18) Mundy, J. A.; Hikita, Y.; Hidaka, T.; Yajima, T.; Higuchi, T.; Hwang, H. Y.; Muller, D. A.; Kourkoutis, L. F. Visualizing The Interfacial Evolution from Charge Compensation to Metallic Screening across the Manganite Metal-Insulator Transition. *Nat. Commun.* **2014**, *5*, 3464.
(19) Meng, Q.; Xu, G.; Xin, H.; Stach, E. A.; Zhu, Y.; Su, D. Quantification of Charge Transfer at the Interfaces of Oxide Thin Films. *J. Phys. Chem. A* **2019**, *123*, 4632−4637.
(20) Gloter, A.; Badjeck, V.; Bocher, L.; Brun, N.; March, K.; Marinova, M.; Tence, M.; Walls, M.; Zobelli, A.; Stephan, O.; Colliex, C. Atomically Resolved Mapping of EELS Fine Structures. *Mater. Sci. Semicond. Process.* **2017**, *65*, 2−17.
(21) Spurgeon, S. R.; Balachandran, P. V.; Kepaptsoglou, D. M.; Damodaran, A. R.; Karthik, J.; Nejati, S.; Jones, L.; Ambaye, H.; Lauter, V.; Ramasse, Q. M.; Lau, K. K. S.; Martin, L. W.; Rondinelli, J. M.; Taheri, M. L. Polarization Screening-Induced Magnetic Phase Gradients at Complex Oxide Interfaces. *Nat. Commun.* **2015**, *6*, 6735.
(22) Song, K.; Ryu, S.; Lee, H.; Paudel, T. R.; Koch, C. T.; Park, B.; Lee, J. K.; Choi, S. Y.; Kim, Y. M.; Kim, J. C.; Jeong, H. Y.; Rzchowski, M. S.; Tsymbal, E. Y.; Eom, C. B.; Oh, S. H. Direct Imaging of the Electron Liquid at Oxide Interfaces. *Nat. Nanotechnol.* **2018**, *13*, 198−203.
(23) Lee, H.; Campbell, N.; Lee, J.; Asel, T. J.; Paudel, T. R.; Zhou, H.; Lee, J. W.; Noesges, B.; Seo, J.; Park, B.; Brillson, L. J.; Oh, S. H.; Tsymbal, E. Y.; Rzchowski, M. S.; Eom, C. B. Direct Observation of a Two-Dimensional Hole Gas at Oxide Interfaces. *Nat. Mater.* **2018**, *17*, 231−236.
(24) Zheng, Q.; Schreiber, N. J.; Zheng, H.; Yan, J.; McGuire, M. A.; Mitchell, J. F.; Chi, M.; Sales, B. C. Real Space Visualization of Competing Phases in $La_{0.6}Sr_{2.4}Mn_2O_7$ Single Crystals. *Chem. Mater.* **2018**, *30*, 7962−7969.
(25) Savitzky, B. H.; El Baggari, I.; Admasu, A. S.; Kim, J.; Cheong, S. W.; Hovden, R.; Kourkoutis, L. F. Bending and Breaking of Stripes in a Charge Ordered Manganite. *Nat. Commun.* **2017**, *8*, 1883.
(26) El Baggari, I.; Savitzky, B. H.; Admasu, A. S.; Kim, J.; Cheong, S. W.; Hovden, R.; Kourkoutis, L. F. Nature and Evolution of Incommensurate Charge Order in Manganites Visualized with Cryogenic Scanning Transmission Electron Microscopy. *Proc. Natl. Acad. Sci. U. S. A.* **2018**, *115*, 1445−1450.
(27) Gao, W.; Addiego, C.; Wang, H.; Yan, X.; Hou, Y.; Ji, D.; Heikes, C.; Zhang, Y.; Li, L.; Huyan, H.; Blum, T.; Aoki, T.; Nie, Y.; Schlom, D. G.; Wu, R.; Pan, X. Real-Space Charge-Density Imaging with Sub-Angstrom Resolution by Four-Dimensional Electron Microscopy. *Nature* **2019**, *575*, 480−484.
(28) Ziatdinov, M.; Banerjee, A.; Maksov, A.; Berlijn, T.; Zhou, W.; Cao, H.; Yan, J.-Q.; Bridges, C. A.; Mandrus, D.; Nagler, S. E.; et al. Atomic-Scale Observation of Structural and Electronic Orders in the Layered Compound α-$RuCl_3$. *Nat. Commun.* **2016**, *7*, 13774.
(29) Cheng, S.; Xu, C.; Deng, S.; Han, M. G.; Bao, S.; Ma, J.; Nan, C.; Duan, W.; Bellaiche, L.; Zhu, Y.; Zhu, J. Interface Reconstruction with Emerging Charge Ordering in Hexagonal Manganite. *Sci. Adv.* **2018**, *4*, No. eaar4298.
(30) Garcia-Barriocanal, J.; Bruno, F. Y.; Rivera-Calzada, A.; Sefrioui, Z.; Nemes, N. M.; Garcia-Hernandez, M.; Rubio-Zuazo, J.; Castro, G. R.; Varela, M.; Pennycook, S. J.; Leon, C.; Santamaria, J. Charge Leakage" at $LaMnO_3/SrTiO_3$ Interfaces. *Adv. Mater.* **2010**, *22*, 627−32.
(31) Wang, H.; Jiang, X.; Wang, Y.; Stark, R. W.; van Aken, P. A.; Mannhart, J.; Boschker, H. Direct Observation of Huge Flexoelectric Polarization around Crack Tips. *Nano Lett.* **2020**, *20*, 88−94.
(32) Kirkland, E. J.; Loane, R. F.; Silcox, J. Simulation of Annular Dark Field Stem Images Using a Modified Multislice Method. *Ultramicroscopy* **1987**, *23*, 77−96.
(33) Langmore, J. The Collection of Scattered Electrons in Dark-Field Electron Microscopy. *Optik* **1973**, *38*, 335−350.
(34) Tomita, K.; Miyata, T.; Olovsson, W.; Mizoguchi, T. Strong Excitonic Interactions in the Oxygen K-edge of Perovskite Oxides. *Ultramicroscopy* **2017**, *178*, 105−111.
(35) Shah, A. B.; Zhai, X.; Jiang, B.; Wen, J.-G.; Eckstein, J. N.; Zuo, J.-M. Electron Energy-Loss Study of the Electronic Structure of Atomic Scale $SrTiO_3$-$SrMnO_3$-$LaMnO_3$ Superlattices. *Phys. Rev. B: Condens. Matter Mater. Phys.* **2008**, *77*, 115103.
(36) Bagues, N.; Santiso, J.; Esser, B. D.; Williams, R. E. A.; McComb, D. W.; Konstantinovic, Z.; Balcells, L.; Sandiumenge, F. The Misfit Dislocation Core Phase in Complex Oxide Heteroepitaxy. *Adv. Funct. Mater.* **2018**, *28*, 1704437.
(37) Zhang, Q.; He, X.; Shi, J.; Lu, N.; Li, H.; Yu, Q.; Zhang, Z.; Chen, L.-Q.; Morris, B.; Xu, Q.; et al. Atomic-Resolution Imaging of Electrically Induced Oxygen Vacancy Migration and Phase transformation in $SrCoO_{2.5-\sigma}$. *Nat. Commun.* **2017**, *8*, 104.
(38) Varela, M.; Oxley, M. P.; Luo, W.; Tao, J.; Watanabe, M.; Lupini, A. R.; Pantelides, S. T.; Pennycook, S. J. Atomic-Resolution Imaging of Oxidation States in Manganites. *Phys. Rev. B: Condens. Matter Mater. Phys.* **2009**, *79*, 085117.
(39) Tan, H. Y.; Verbeeck, J.; Abakumov, A.; Van Tendeloo, G. Oxidation State and Chemical Shift Investigation in Transition Metal Oxides by EELS. *Ultramicroscopy* **2012**, *116*, 24−33.
(40) Kobayashi, S.; Tokuda, Y.; Mizoguchi, T.; Shibata, N.; Sato, Y.; Ikuhara, Y.; Yamamoto, T. Quantitative Analyses of Oxidation States for Cubic $SrMnO_3$ and Orthorhombic $SrMnO_{2.5}$ with Electron Energy Loss Spectroscopy. *J. Appl. Phys.* **2010**, *108*, 124903.
(41) Borisevich, A. Y.; Chang, H. J.; Huijben, M.; Oxley, M. P.; Okamoto, S.; Niranjan, M. K.; Burton, J. D.; Tsymbal, E. Y.; Chu, Y. H.; Yu, P.; Ramesh, R.; Kalinin, S. V.; Pennycook, S. J. Suppression of Octahedral Tilts and Associated Changes in Electronic Properties at Epitaxial Oxide Heterostructure Interfaces. *Phys. Rev. Lett.* **2010**, *105*, 087204.
(42) Hytch, M. J.; Snoeck, E.; Kilaas, R. Quantitative Measurement of Displacement and Strain Fields from HREM Micrographs. *Ultramicroscopy* **1998**, *74*, 131−146.
(43) Hytch, M. J.; Minor, A. M. Observing and Measuring Strain in Nanostructures and Devices with Transmission Electron Microscopy. *MRS Bull.* **2014**, *39*, 138−146.
(44) Wang, Y.; Salzberger, U.; Sigle, W.; Eren Suyolcu, Y.; van Aken, P. A. Oxygen Octahedra Picker: A Software Tool to Extract Quantitative Information from STEM Images. *Ultramicroscopy* **2016**, *168*, 46−52.
(45) Zhang, Y.; Shen, L.; Liu, M.; Li, X.; Lu, X.; Lu, L.; Ma, C.; You, C.; Chen, A.; Huang, C.; et al. Flexible Quasi-Two-Dimensional $CoFe_2O_4$ Epitaxial Thin Films for Continuous Strain Tuning of Magnetic Properties. *ACS Nano* **2017**, *11*, 8002−8009.
(46) Clément, L.; Pantel, R.; Kwakman, L. T.; Rouvière, J. Strain Measurements by Convergent-Beam Electron Diffraction: The Importance of Stress Relaxation in Lamella Preparations. *Appl. Phys. Lett.* **2004**, *85*, 651−653.
(47) Cooper, D.; Denneulin, T.; Bernier, N.; Béché, A.; Rouvière, J.-L. Strain Mapping of Semiconductor Specimens with nm-Scale Resolution in a Transmission Electron Microscope. *Micron* **2016**, *80*, 145−165.

https://dx.doi.org/10.1021/acsnano.0c01545
ACS Nano 2020, 14, 12697−12707

(48) Cherkashin, N.; Denneulin, T.; Hÿtch, M. J. Electron Microscopy by Specimen Design: Application to Strain Measurements. *Sci. Rep.* **2017**, *7*, 12394.
(49) Becher, C.; Maurel, L.; Aschauer, U.; Lilienblum, M.; Magen, C.; Meier, D.; Langenberg, E.; Trassin, M.; Blasco, J.; Krug, I. P.; Algarabel, P. A.; Spaldin, N. A.; Pardo, J. A.; Fiebig, M. Strain-Induced Coupling of Electrical Polarization and Structural Defects in $SrMnO_3$ Films. *Nat. Nanotechnol.* **2015**, *10*, 661−5.
(50) Choi, S. Y.; Kim, S. D.; Choi, M.; Lee, H. S.; Ryu, J.; Shibata, N.; Mizoguchi, T.; Tochigi, E.; Yamamoto, T.; Kang, S. J.; Ikuhara, Y. Assessment of Strain-Generated Oxygen Vacancies Using $SrTiO_3$ Bicrystals. *Nano Lett.* **2015**, *15*, 4129−34.
(51) Lee, J. H.; Rabe, K. M. Epitaxial-Strain-Induced Multiferroicity in $SrMnO_3$ from First Principles. *Phys. Rev. Lett.* **2010**, *104*, 207204.
(52) Aschauer, U.; Pfenninger, R.; Selbach, S. M.; Grande, T.; Spaldin, N. A. Strain-Controlled Oxygen Vacancy Formation and Ordering in $CaMnO_3$. *Phys. Rev. B: Condens. Matter Mater. Phys.* **2013**, *88*, 054111.
(53) Agrawal, P.; Guo, J.; Yu, P.; Hebert, C.; Passerone, D.; Erni, R.; Rossell, M. D. Strain-Driven Oxygen Deficiency in Multiferroic $SrMnO_3$ Thin Films. *Phys. Rev. B: Condens. Matter Mater. Phys.* **2016**, *94*, 104101.
(54) Chu, M. W.; Liou, S. C.; Chang, C. P.; Choa, F. S.; Chen, C. H. Emergent Hemical Mapping at Atomic-Column Resolution by Energy-Dispersive X-Ray Spectroscopy in an Aberration-Corrected Electron Microscope. *Phys. Rev. Lett.* **2010**, *104*, 196101.
(55) Egerton, R.; Yang, Y.-Y.; Chen, F. EELS of "Thick" Specimens. *Ultramicroscopy* **1991**, *38*, 349−352.
(56) Malis, T.; Cheng, S. C.; Egerton, R. F. EELS Log-Ratio Technique for Specimen-Thickness Measurement in the TEM. *J. Electron Microsc. Tech.* **1988**, *8*, 193−200.
(57) Allen, L. J. Simulation in Elemental Mapping using Aberration-Corrected Electron Microscopy. *Ultramicroscopy* **2017**, *180*, 142−149.
(58) Allen, L.J.; D'Alfonso, A.J.; Findlay, S.D. Modelling the Inelastic Scattering of Fast Electrons. *Ultramicroscopy* **2015**, *151*, 11−22.
(59) Kourkoutis, L. F.; Song, J. H.; Hwang, H. Y.; Muller, D. A. Microscopic Origins for Stabilizing Room-Temperature Ferromagnetism in Ultrathin Manganite Layers. *Proc. Natl. Acad. Sci. U. S. A.* **2010**, *107*, 11682−5.
(60) Maurel, L.; Marcano, N.; Prokscha, T.; Langenberg, E.; Blasco, J.; Guzman, R.; Suter, A.; Magen, C.; Morellon, L.; Ibarra, M. R.; Pardo, J. A.; Algarabel, P. A. Nature of Antiferromagnetic Order in Epitaxially Strained Multiferroic $SrMnO_3$ Thin Films. *Phys. Rev. B: Condens. Matter Mater. Phys.* **2015**, *92*, 024419.
(61) Shannon, R. D. Revised Effective Ionic-Radii and Systematic Studies of Interatomic Distances in Halides and Chalcogenides. *Acta Crystallogr., Sect. A: Cryst. Phys., Diffr., Theor. Gen. Crystallogr.* **1976**, *32*, 751−767.
(62) Guzman, R.; Maurel, L.; Langenberg, E.; Lupini, A. R.; Algarabel, P. A.; Pardo, J. A.; Magen, C. Polar-Graded Multiferroic $SrMnO_3$ Thin Films. *Nano Lett.* **2016**, *16*, 2221−2227.
(63) Nord, M.; Vullum, P. E.; Moreau, M.; Boschker, J. E.; Selbach, S. M.; Holmestad, R.; Tybell, T. Structural Phases Driven by Oxygen Vacancies at the $La_{0.7}Sr_{0.3}MnO_3/SrTiO_3$ Hetero-Interface. *Appl. Phys. Lett.* **2015**, *106*, 041604.
(64) Chandrasena, R. U.; Yang, W.; Lei, Q.; Delgado-Jaime, M. U.; Wijesekara, K. D.; Golalikhani, M.; Davidson, B. A.; Arenholz, E.; Kobayashi, K.; Kobata, M.; de Groot, F. M.; Aschauer, U.; Spaldin, N. A.; Xi, X.; Gray, A. X. Strain-Engineered Oxygen Vacancies in $CaMnO_3$ Thin Films. *Nano Lett.* **2017**, *17*, 794−799.
(65) Nakamura, M.; Sawa, A.; Fujioka, J.; Kawasaki, M.; Tokura, Y. Interface Band Profiles of Mott-Insulator/Nb: $SrTiO_3$ Heterojunctions as Investigated by Optical Spectroscopy. *Phys. Rev. B: Condens. Matter Mater. Phys.* **2010**, *82*, 201101.
(66) Chen, Y.; Gan, Y.; Christensen, D. V.; Zhang, Y.; Pryds, N. Effect of Sr-Doping of $LaMnO_3$ Spacer on Modulation-Doped Two-Dimensional Electron Gases at Oxide Interfaces. *J. Appl. Phys.* **2017**, *121*, 095305.
(67) Lin, X.; Bridoux, G.; Gourgout, A.; Seyfarth, G.; Krämer, S.; Nardone, M.; Fauqué, B.; Behnia, K. Critical Doping for the Onset of a Two-Band Superconducting Ground State in $SrTiO_{3-\delta}$. *Phys. Rev. Lett.* **2014**, *112*, 207002.
(68) Scullin, M. L.; Ravichandran, J.; Yu, C.; Huijben, M.; Seidel, J.; Majumdar, A.; Ramesh, R. Pulsed Laser Deposition-Induced Reduction of $SrTiO_3$ Crystals. *Acta Mater.* **2010**, *58*, 457−463.
(69) Schneider, C. W.; Döbeli, M.; Richter, C.; Lippert, T. Oxygen Diffusion in Oxide Thin Films Grown on $SrTiO_3$. *Phys. Rev. Mater.* **2019**, *3*, 123401.
(70) Maier, J. Ionic Conduction in Space Charge Regions. *Prog. Solid State Chem.* **1995**, *23*, 171−263.
(71) Baiutti, F.; Logvenov, G.; Gregori, G.; Cristiani, G.; Wang, Y.; Sigle, W.; van Aken, P. A.; Maier, J. High-Temperature Superconductivity in Space-Charge Regions of Lanthanum Cuprate Induced by Two-Dimensional Doping. *Nat. Commun.* **2015**, *6*, 8586.
(72) De Souza, R. A. The Formation of Equilibrium Space-Charge Zones at Grain Boundaries in the Perovskite Oxide $SrTiO_3$. *Phys. Chem. Chem. Phys.* **2009**, *11*, 9939−9969.
(73) Koster, G.; Kropman, B. L.; Rijnders, G. J. H. M.; Blank, D. H. A.; Rogalla, H. Quasi-Ideal Strontium Titanate Crystal Surfaces through Formation of Strontium Hydroxide. *Appl. Phys. Lett.* **1998**, *73*, 2920−2922.
(74) Cueva, P.; Hovden, R.; Mundy, J. A.; Xin, H. L.; Muller, D. A. Data Processing for Atomic Resolution Electron Energy Loss Spectroscopy. *Microsc. Microanal.* **2012**, *18*, 667−675.
(75) Koch, C. T. Determination of Core Structure Periodicity and Point Defect Density along Dislocations. Doctoral dissertation, Arizona State University, 2002.
(76) Cuong, D. D.; Lee, B.; Choi, K. M.; Ahn, H.-S.; Han, S.; Lee, J. Oxygen Vacancy Clustering and Electron Localization in Oxygen-Deficient $SrTiO_3$: LDA + U Study. *Phys. Rev. Lett.* **2007**, *98*, 115503.

https://dx.doi.org/10.1021/acsnano.0c01545
ACS Nano 2020, 14, 12697−12707